### **PAPER • OPEN ACCESS**

## Effects of the thrust force induced by wind turbine rotors on the incoming wind field: A wind LiDAR experiment

To cite this article: Stefano Letizia et al 2022 J. Phys.: Conf. Ser. 2265 022033

View the article online for updates and enhancements.

## You may also like

- Rapid, high-resolution measurement of leaf area and leaf orientation using terrestrial LiDAR scanning data
  Brian N Bailey and Walter F Mahaffee
- Geodetic imaging with airborne LiDAR: the Earth's surface revealed C L Glennie, W E Carter, R L Shrestha et al
- Remote assessment of extracted volumes and greenhouse gases from tropical timber harvest

Timothy R H Pearson, Blanca Bernal, Stephen C Hagen et al.



**2265** (2022) 022033

doi:10.1088/1742-6596/2265/2/022033

# Effects of the thrust force induced by wind turbine rotors on the incoming wind field: A wind LiDAR experiment

Stefano Letizia<sup>1</sup>, Coleman Moss<sup>1</sup>, Matteo Puccioni<sup>1</sup>, Clément Jacquet<sup>2</sup>, Dale Apgar<sup>2</sup>, Giacomo Valerio Iungo<sup>1,\*</sup>

[1] Center for Wind Energy, Mechanical Engineering Department, The University of Texas at Dallas

[2] GE Renewables

E-mail: valerio.iungo@utdallas.edu

Abstract. A field experiment was conducted to investigate the effects of the thrust force induced by utility-scale wind turbines on the incoming wind field. Five wind profiling LiDARs and a scanning Doppler pulsed wind LiDAR were deployed in the proximity of a row of four wind turbines located over relatively flat terrain, both before and after the construction of the wind farm. The analysis of the LiDAR data collected during the pre-construction phase enables quantifying the wind map of the site, which is then leveraged to correct the post-construction LiDAR data and isolate rotor-induced effects on the incoming wind field. The analysis of the profiling LiDAR data allows for the identification of the induction zone upstream of the turbine rotors, with an increasing velocity deficit moving from the top tip towards the bottom tip of the rotor. The largest wind speed reduction (about 5%) is observed for convective conditions and incoming hub-height wind speed between cut-in and rated wind speeds. The scanning LiDAR data indicate the presence of speedup regions within the gaps between adjacent turbine rotors. Speedup increases with reducing the transverse distance between the rotors, atmospheric instability (maximum 15%), while a longer streamwise extent of the speedup region is observed under stable atmospheric conditions.

### 1. Introduction

For research on the wind flow field associated with wind turbines and wind farms, major attention has been generally paid to the wakes generated and their effects on power capture and structural loads of wind turbines (e.g., [1, 2, 3, 4]). More recently, the wind energy science community has recognized the importance of the pressure field associated with the rotor thrust force, which can modify the incoming atmospheric boundary layer (ABL), specifically reducing the rotor equivalent velocity, and leading to small yet noticeable under-performance in terms of power capture. This physical process has been typically dubbed as wind farm blockage, as documented through numerical simulations [5], yet a few field campaigns were performed for its characterization [6, 7].

Besides wind turbine and wind farm blockage, the perturbation induced by the rotor thrust on the incoming ABL can also lead to local speedup regions, especially when other turbine rotors are located nearby. Speedup regions have been observed numerically and through wind tunnel experiments [8, 9, 10], while extensive field experimental evidence is still lacking.

Content from this work may be used under the terms of the Creative Commons Attribution 3.0 licence. Any further distribution of this work must maintain attribution to the author(s) and the title of the work, journal citation and DOI.

**2265** (2022) 022033

doi:10.1088/1742-6596/2265/2/022033

Understanding pressure-induced effects on wind farm performance is also important in light of the local speed enhancement for turbine arrays, as reported in theoretical [8], numerical [9, 10], and wind tunnel studies [11], which clashed with the power losses observed for real wind farms [6, 11]. Further, the role of atmospheric stratification on rotor-induced effects of the incoming wind is still not clearly understood, yet recent studies showed more severe flow modifications occurring under stable atmospheric conditions as a consequence of the vertical flow confinement due to a smaller boundary layer height and gravity waves [12, 13].

For this work, a field campaign was carried out for a utility-scale wind farm to detect and quantify the effect of the rotor thrust and the associated pressure field on the incoming wind field. Five profiling light and detection and ranging (LiDAR) units were deployed in different phases before and after the construction of a wind farm to characterize the wind field investing and surrounding the wind turbine rotors. After the commissioning of the farm, a scanning Doppler pulsed wind LiDAR was added to the setup upstream of an array of four wind turbines according to the prevailing wind direction [14, 15, 16]. The main experimental goal of the scanning LiDAR is to probe the induction zone and the wakes, including the speed-up area, continuously for a period of two months.

The remainder of this paper is structured as follows. The setup of the experiment is described in Sect. 2, together with the design of the LiDAR measurements, and the quantification of the LiDAR measurement accuracy. The analysis of the measurements performed to identify the effects induced by the turbine rotor thrust on the incoming wind field is organized in results from the profiling LiDARs (Sect. 3.1), and the scanning LiDAR (Sect. 3.2). Finally, concluding remarks are reported in Sect. 4.

2. Field experiment to investigate rotor-induced effects on the incoming wind field Figure 1-a illustrates the experimental site under investigation with the relevant instrumentation. The experimental site is located in the northwest of the United States over relatively flat terrain. The locations of the profiling LiDARs (PL) and scanning LiDAR (SL) are there reported together with the turbine locations (T).

The turbines investigated have a rotor diameter of  $D=127\,\mathrm{m}$  and a hub height of  $H=89\,\mathrm{m}$ . Supervisory control and data acquisition (SCADA) data were made available as ten-minute statistics (mean and standard deviation) of hub height wind speed, temperature, active power, thrust, generator RPM, and RPM set-point. For this particular study, only turbines T06-T09 are considered.

As can be seen from the wind rose, the wind direction is dominated by WSW directions, which means that the available instrumentation is generally located upwind of the turbine rotors to characterize their induction zones. The site climatology is primarily driven by a diurnal cycle of atmospheric stability, as indicated in figure 1-b by the turbulence intensity at hub height,  $TI_{\infty}$ , recorded from the SCADA for the different times of the day. For this analysis, wake conditions are removed according to the 61400-12, Annex B of the IEC standards. It is observed that on average  $TI_{\infty}$  can achieve values larger than 10% for daytime convective conditions, while for nighttime stable conditions it can be lower than 5%. Effects of the daily cycle of atmospheric stability are also well captured from the analysis of the wind veer and shear. In figure 2, the average variability in wind speed and wind direction over height is reported for the different times of the day. Wind shear is enhanced during nighttime stable conditions while significant wind veer occurs as well across the rotor heights.

For this experiment, five profiling LiDARs were deployed, specifically Windcube V2 profiling LiDARs. Doppler beam swinging (DBS) measurements were performed with the profiling LiDARs using a scanning cone half-angle of  $28^{\circ}$  to provide ten-minute averaged wind speed and direction at the heights of 40 m, 64 m, 89 m, 114 m, 140 m, 153 m, 160 m, 180 m, 200 m. PL04 is aimed at measuring the inflow for the prevalent wind direction; PL02 and PL01 characterize

**2265** (2022) 022033

doi:10.1088/1742-6596/2265/2/022033

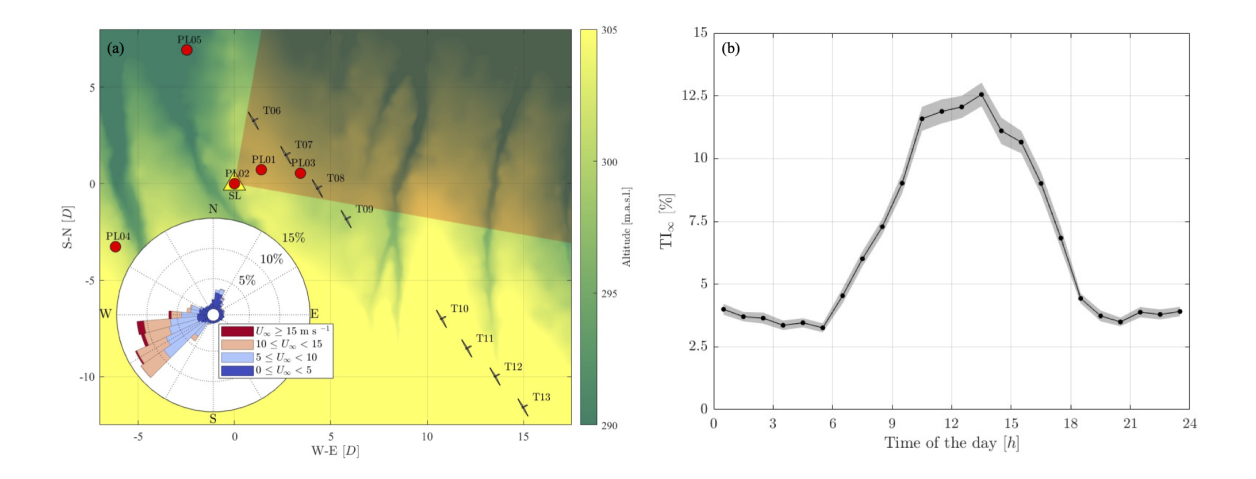
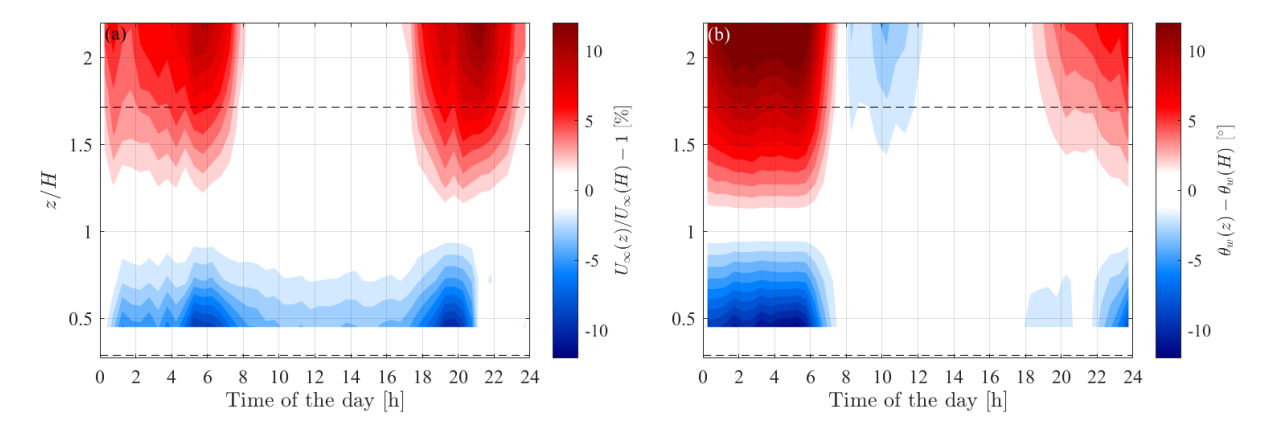


Figure 1. Experimental site: (a) Map of the wind farm (PL=profiling LiDAR, SL=scanning LiDAR, T=turbine). The wind rose is based on hub-height wind data averaged among all the profiling LiDARs during the pre-construction phase. The shaded sector indicates the area probed by the scanning LiDAR. (b) Daily cycle of hub-height turbulence intensity measured from the nacelle anemometers and averaged over unwaked turbines during the post-construction phase of the experiment. The shaded area indicates error on the mean at a 95% confidence level.



**Figure 2.** Vertical variability of wind resource from pre-construction profiling LiDAR data: (a) percentage deviation of wind speed (shear); (b) deviation of wind direction (veer). The dashed lines represent the bottom- and top-tip height.

the flow 2D and 1D upstream of the turbine row; PL03 was placed to probe the flow between T07 and T08; PL05 is a backup LiDAR deployed to guarantee redundancy; SL, a Windcube 200S scanning Doppler pulsed wind LiDAR, was used for volumetric wind measurements.

This project was carried out in three different phases. During phase 1, five profiling LiDARs were installed to characterize the spatial variability of the background wind field for different wind directions and atmospheric stability regimes. This phase was conducted before the installation of the wind turbines during the period from June 18, 2020, until August 11, 2020. During phase 2, the five profiling LiDARs were collocated to quantify the accuracy of the instruments. Data were collected from August 12, 2020, to September 30, 2020. This phase also occurred during the installation of the turbines. Finally, phase 3 was conducted from December

**2265** (2022) 022033

doi:10.1088/1742-6596/2265/2/022033

15, 2020, to June 14, 2021, following the installation of the turbines. This phase used the five profiling LiDARs, returned to their original locations, as well as a scanning wind LiDAR, to measure pressure effects induced by the turbines. The final locations of all turbines and instruments are noted in figure 1. Phase 1 locations for the profiling LiDARs are identical to the phase 3 locations noted in the figure.

The scanning strategy for the scanning LiDAR was optimally designed through the LiDAR Statistical Barnes Objective Analysis (LiSBOA) [17] to quantify the hub-height mean velocity with fundamental half-wavelengths of  $\Delta n_x = 1D$  and  $\Delta n_y = 0.5D$  in the streamwise and spanwise directions, respectively, which are deemed to be adequate to spatially resolve flow features of the induction zone and the near-wake (more details available in [18]). With the logistic constraint of the scanning wind LiDAR located 3D upwind of the wind turbines under investigation for the prevailing WSW wind directions, the optimal scan maximizing the coverage of the target volume (70% of the domain adequately sampled) and the statistical convergence (error on the mean of 0.4 m s<sup>-1</sup>) includes 5 planar position indicator (PPI) scans with a range gate of 50 m, elevation angles of the LiDAR laser beam of [3.42°, 4.39°, 6.13°, 10.13°, 27.95°] spanning the azimuthal range [10°, 100°] with a 2° angular resolution in the azimuthal direction, resulting in a total sampling time of 112 s.

The instrumental uncertainty of the profiling LiDARs is assessed by comparing the data collected in phase 2 of the project. Data are preliminarily filtered by removing samples characterized by a carrier-to-noise ratio (CNR) lower than -21 dB. Specifically, a linear fit of the 10-minute-averaged horizontal wind speed at all heights for each LiDAR pair is performed. More than 5000 valid samples ( $\sim 35$  days) are available at all gates. From the linear regression among the different heights, the largest deviation from unit correlation is quite small (< 0.2% for PL05), which indicates that the inter-correlation coefficient is always included in the range [0.998, 1.002] for all LiDARs and all heights. Modest deviation from the unit slope (< 1.5%) and intercept ( $< 0.2 \text{ m s}^{-1}$ ) are also observed, which suggests that all the LiDARs have negligible bias and random cross-error compared to the statistical uncertainty for the present analysis.

### 3. Results

### 3.1. Analysis of the wind data collected from the profiling LiDARs

In this section, wind data collected from profiling LiDARs are analyzed with a dual goal: i) characterize the background flow heterogeneity over the site at hub height using data collected during phase 1 of the project; ii) investigate the effects of the turbine rotor thrust on the incoming wind field. To these aims, we define the horizontal wind speed difference between each LiDAR and the reference LiDAR PL04, which is located further upwind for the prevailing WSW wind directions, as:

$$\Delta U_i(z) = \frac{U_i(z) - U_4(z)}{U_4(z)}.$$
 (1)

For the characterization of the background flow during the pre-construction phase of the project, the wind speed difference is bin-averaged as a function of wind direction for  $10^{\circ}$ -wide wind sectors, separately for daytime (between 6:00 and 18:00 local time) and nighttime (between 18:00 and 6:00 local time), and for region II operations ( $U_{\text{norm},\infty} \in (0.4, 0.75]$ , where  $U_{\text{norm},\infty}$  is the density-corrected hub height wind speed made non-dimensional with the turbine rated wind speed [19]).

In figure 3, the directional average of  $\Delta U$  is shown for the various wind sectors, and daytime and nighttime periods for PL01, PL02, PL03. It is noteworthy that the variability of the unperturbed background flow, which is affected by the site topography for specific wind/atmospheric conditions, can have a magnitude comparable to the wind speed reduction connected with wind turbine blockage [6]. Therefore, for field experiments aiming at investigating wind turbine/farm blockage, it is important that background flow gradients are

**2265** (2022) 022033

doi:10.1088/1742-6596/2265/2/022033

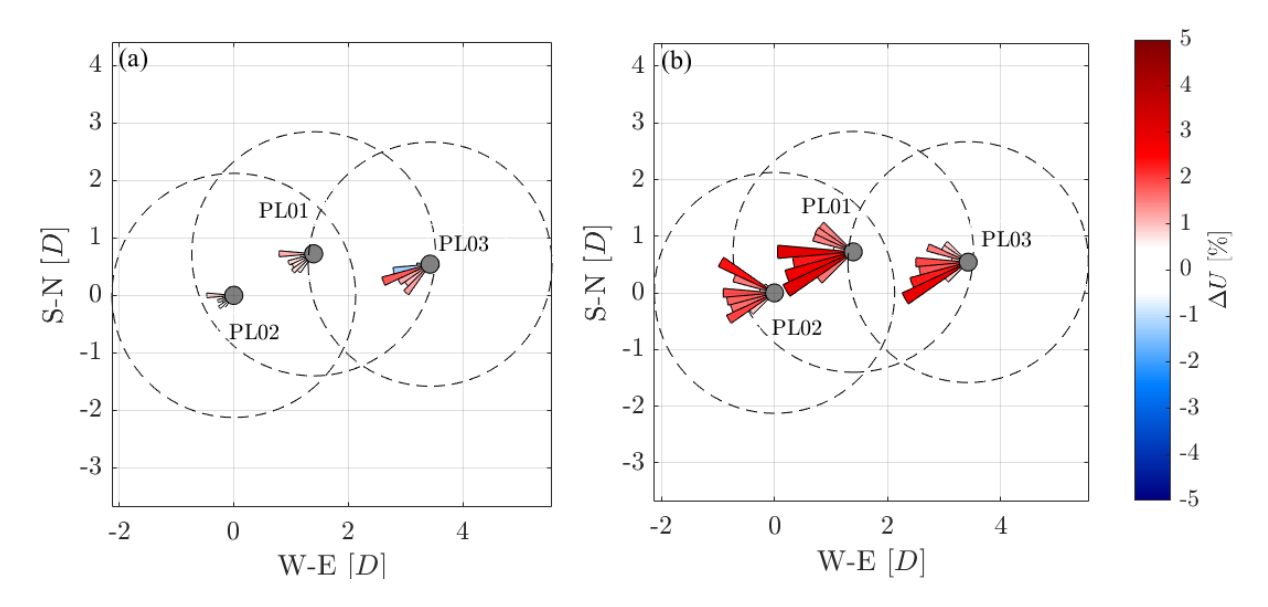


Figure 3. Background flow analysis for phase 1 and  $U_{\text{norm},\infty} \in (0.4, 0.75]$ : (a) directional average of  $\Delta U$  nighttime; (b) directional average of  $\Delta U$  daytime. Sectors with standard error on the mean higher than 5% with 95% confidence level are discarded.

properly quantified and removed before analyzing this wind farm flow feature from wind data. For this work, streamwise and spanwise wind velocity gradients are quantified through a bilinear fitting of the sectorial averages of  $\Delta U$ , which will be then accounted for in the following analysis.

In the light of these considerations, the blockage effect is quantified from the profiling LiDAR data by calculating the average difference between  $\Delta U$  measured during phase 3 (which includes wind farm and background flow effects together) and that of phase 1 (only background flow effects) and for all the heights and regions of the power curve. Furthermore, the statistical significance is enhanced by averaging all data from the WSW wind sector ( $\theta_w \in (201, 270]$ ), which is possible thanks to the non-dimensional nature of  $\Delta U$ . Figure 4 shows the corrected wind speed deviation separately for each profiling LiDAR, three different regions of the power curve, and nighttime and daytime operations. The wind speed shows a noticeable reduction throughout the rotor heights, which is enhanced by moving downwards. For daytime, this effect is enhanced for low  $U_{\text{norm},\infty}$  values (i.e high  $c_t$  for region II operations), which corroborates the hypothesis that slowdown is induced by the turbine rotor thrust.

Nighttime conditions are still characterized by lower wind speeds by up to 4% after the construction of the farm, although the dependence on  $U_{\text{norm},\infty}$  (i.e.  $c_t$ ) is less clear. We argue that the effect of stable stratification and the associated strong wind shear and veer induce more complex 3D effects on the wind field, which are difficult to characterize with profiling LiDARs, which assume horizontal homogeneity over each measurement volume. Nonetheless, data collected for both daytime and nighttime operations confirm a general wind speed reduction over the rotor heights, with a maximum deceleration at lower heights investigated and reducing roughly monotonically approaching the top-tip of the rotor, as previously indicated from both experiments and numerical simulations [20, 21, 22].

Aloft the rotor top tip, speedups are generally observed with a magnitude of about 1%. Therefore, combining these flow features together, namely velocity reduction over the rotor enhanced with reducing height, speedup aloft rotor top tip, might suggest that the rotor is

**2265** (2022) 022033

doi:10.1088/1742-6596/2265/2/022033

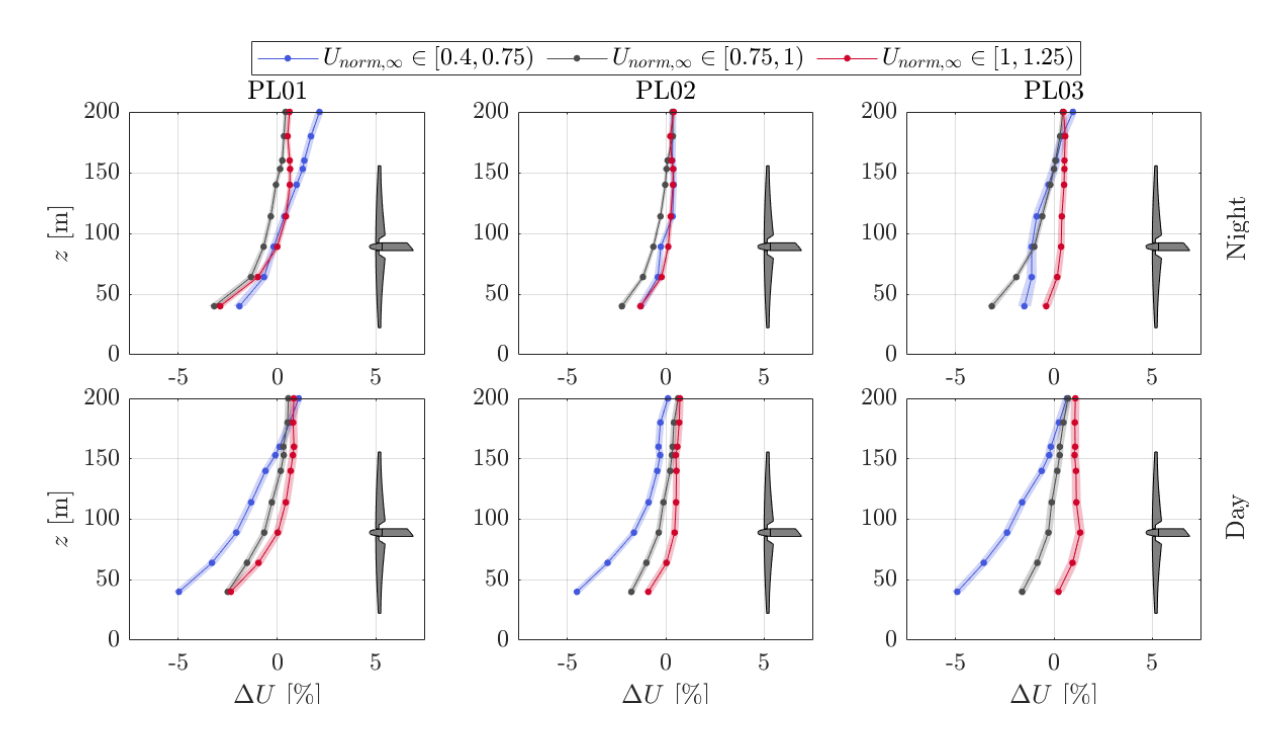


Figure 4. Difference of  $\Delta U$  between phase 3 (post-construction) and phase 1 (pre-construction) for nighttime (top row) and daytime (bottom row), and different regions of the power curve (see colors in the legend). The shaded area indicates error on the mean at a 95% confidence level.

affecting the incoming wind through a bluff-body-like behavior. The wind field is decelerated in correspondence of the rotor area and accelerated over the surrounding area to circumvent the rotor. Nonetheless, the three-dimensional features of the incoming atmospheric boundary layer and the rotation of the wind turbine blades make this flow much more complex than those associated with classical bluff bodies. Furthermore, it should be considered that the blockage induced by the turbines, especially if deployed as an array, may lead to an abrupt transition in the terrain aerodynamic roughness and generation of an internal boundary layer, which makes this flow scenario even more complex. More extensive and accurate measurements are needed to address these discussions, which remain mainly speculative.

### 3.2. Analysis of the wind data collected from the scanning wind LiDAR

Data collected from a scanning Doppler pulsed wind LiDAR are objectively analyzed to gain insight into the velocity field around the turbines with the ultimate goal of detecting and quantifying pressure-induced effects connected with the thrust force of the turbine rotor. Quality control of the raw LiDAR data is performed using the dynamic filter [23]. Subsequently, the hubheight wind direction,  $\theta_w$ , and the vertical wind profile,  $U_{\infty}(z)$ , measured by PL04 are utilized to calculate the streamwise equivalent velocity and normalize the velocity field by dividing the streamwise equivalent velocity by the incoming boundary layer profile [4]. The so-obtained shear-corrected, normalized streamwise velocity data are then clustered in 10°-wide sectors of the wind direction. Only data collected during normal turbine operations and region II of the power curve  $(U_{\text{norm},\infty} \in 0.4, 0.75]$ ) are considered. Off-design operations are discarded based on the nominal RPM reported in the SCADA readings. Furthermore, data are analyzed separately for nighttime and daytime due to the strong daily cycle of the wind resource, as discussed in Section 2.

**2265** (2022) 022033

doi:10.1088/1742-6596/2265/2/022033

The 3D probability density function of the LiDAR measurements as a function of  $(U_{\text{norm},\infty}, \theta_w, TI_{\infty})$  is reported in figure 5 with the edges of the selected clusters superposed with green lines. For this study, four and five clusters have been selected for nighttime and daytime, respectively. The centroid of each cluster is indicated with a green cross, showing that nighttime data are confined within a region with  $TI_{\infty} < 10\%$ , while daytime data cover a broader range of  $TI_{\infty}$  up to 25%. It is noteworthy that  $TI_{\infty}$  does not exhibit a significant correlation with  $U_{\text{norm},\infty}$ , as observed, for instance, for offshore wind due to the enhanced effects induced by higher waves generated with larger wind speed [24]. In contrast,  $TI_{\infty}$  seems mainly associated with atmospheric stability, confirming previous investigations for wind farms in flat terrain [4], even though a direct characterization of the atmospheric stability is not provided for this experiment.

Normalized and clustered data should meet the requirement of statistical homogeneity [4, 18], which allows using the LiSBOA tool [17] to reconstruct the low-pass filtered mean velocity fields on a Cartesian grid at hub height. To this aim, the pre-conditioned LiDAR data collected within the vertical range  $z \in (H - D/4, H + D/4)$  are fed to the LiSBOA algorithm using a smoothing parameter of the Barnes scheme  $\sigma = 1/3$ , and the fundamental half-wavelengths provided in Section 2. The results of this analysis are displayed in figure 6 for all the clusters. The wake morphology exhibits a remarkable difference between nighttime and daytime, with longer wakes occurring during stable atmospheric conditions compared to unstable cases [2, 4, 25, 26, 27]. Wakes also appear less symmetric at night, which can likely be a consequence of larger shear and veer that combined with the wake rotation can give arise to uneven momentum mixing [4] and skewed wake shape [28]. Such 3D wake effects are not fully captured by the present scan, which deliberately targets a characterization of the wake velocity field over the horizontal plane at hub height, and would require a more refined and time-consuming volumetric scan, which was not considered during the design of the experiment due to the lower number of scans obtainable and, thus, lower statistical accuracy.

A careful inspection of the velocity fields in figure 6 reveals consistent speedup regions occurring between the turbines, which are a signature of the channeling effect induced by the turbine pressure field and the turbine wakes. This higher momentum zone is particularly evident for more westerly wind directions and its extension appears to be affected by atmospheric stability. To delve deeper into this flow feature, the streamwise velocity fields are extracted along three transects between the turbines, as shown in figure 6. The regular spacing between the

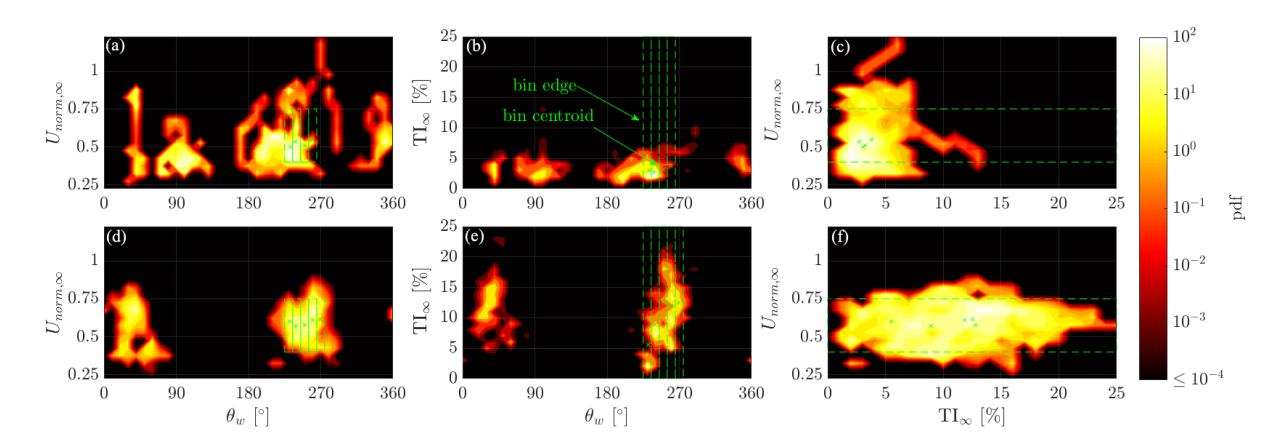


**Figure 5.** Probability density function of the inflow wind conditions: (a) nighttime,  $U_{\text{norm},\infty}$  and  $\theta_w$ ; (b) nighttime,  $TI_{\infty}$  and  $\theta_w$ ; (c) nighttime,  $U_{\text{norm},\infty}$  and  $TI_{\infty}$ ; (d,e,f) same as upper row but for daytime.

**2265** (2022) 022033

doi:10.1088/1742-6596/2265/2/022033

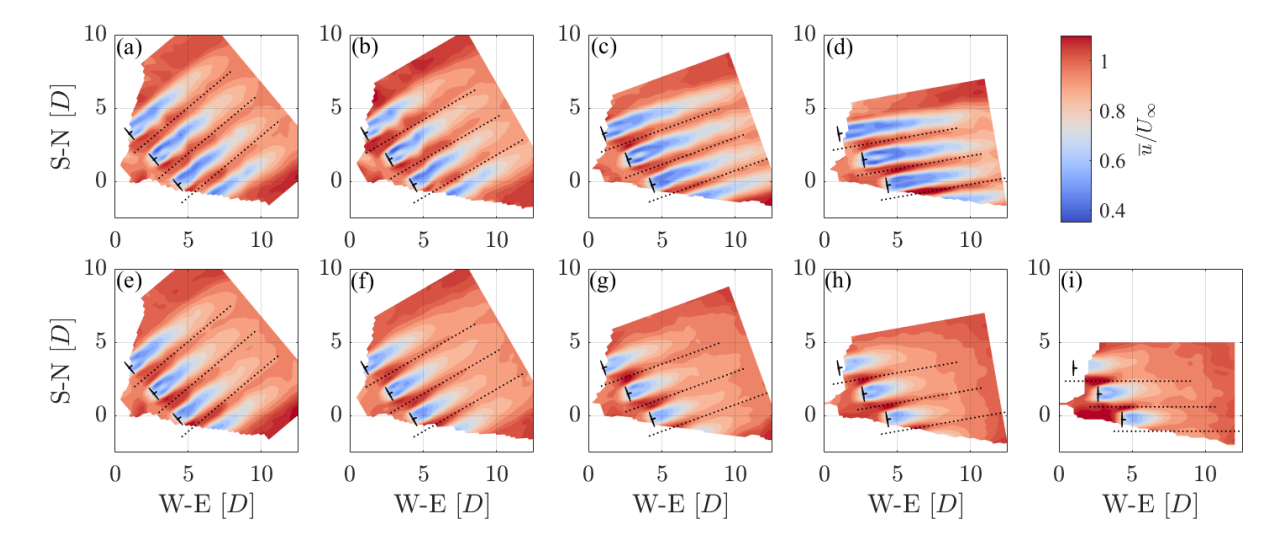


**Figure 6.** Streamwise normalized mean velocity fields for different wind sectors and time of the day: (a-d) nighttime; (e-i): daytime; (a,e)  $\theta_w \in (225, 235]^{\circ}$ ; (b,f)  $\theta_w \in (235, 245]^{\circ}$ ; (c,g)  $\theta_w \in (245, 255]^{\circ}$ ; (d,h)  $\theta_w \in (255, 255]^{\circ}$ ; (i)  $\theta_w \in (265, 275]^{\circ}$ .

turbines allows assuming statistical homogeneity among the different transects. The sampled velocity data are then shifted to the streamwise location of the most upstream turbine for each transect,  $x_0$ , and averaged together (figure 7). The maximum speedup increases consistently as a function of the wind direction moving from SW to W, a likely consequence of the reduced gap between the rotors that enhances the convergence of the streamlines. Further, the location of the speedup region seems to shift downstream with respect to the location of the leading turbine. The speedup region extends further downstream during nighttime than daytime, due to the more elongated wakes observed during low TI, stable conditions. This feature confirms that speedups are linked to mass conservation, which creates high momentum region due to the confinement induced by adjacent wakes. It is noteworthy that the maximum speedup occurs for daytime and westerly wind, and peaks at the remarkable value of 15% (figure 8-a), which is larger than what was observed previously through wind tunnel studies, e.g. 7% with a transverse turbine spacing of 1.25D [11], and numerical simulations, e.g. 3% with a transverse turbine spacing of 3D [10]. The maximum speedup factor decreases fairly linearly as a function of the gap between the turbines, with higher values observed during daytime. This higher speedup observed during unstable conditions is quite surprising considering the stronger vertical flow confinement expected at nighttime stable atmospheric conditions, although it may be a result of the more rapid wake expansion caused by turbulent mixing.

A quantitative insight is gained by evaluating the maximum speedup factor and the center of gravity of the speedup region. The latter is defined as:

$$\operatorname{CoG} = \frac{\int_{S} (\overline{u}/U_{\infty} - 1)(x - x_{0})dx}{\int_{S} (\overline{u}/U_{\infty} - 1)dx}, \quad S = \{x | x \in \mathbb{R}, (\overline{u}/U_{\infty} - 1) > 0\},$$
 (2)

and provides a quantitative indicator of the speedup location. In figure 8-b, the center of gravity of the speedup region also presents an inverse proportionality with the gap, although the trend is non-linear. Further, the speedup shifts more downstream during the night due to the lower turbulent mixing, which results in elongated wake features and thus more persistent speedup regions. It is noteworthy that the speedup center of gravity is generally located at

**2265** (2022) 022033

doi:10.1088/1742-6596/2265/2/022033

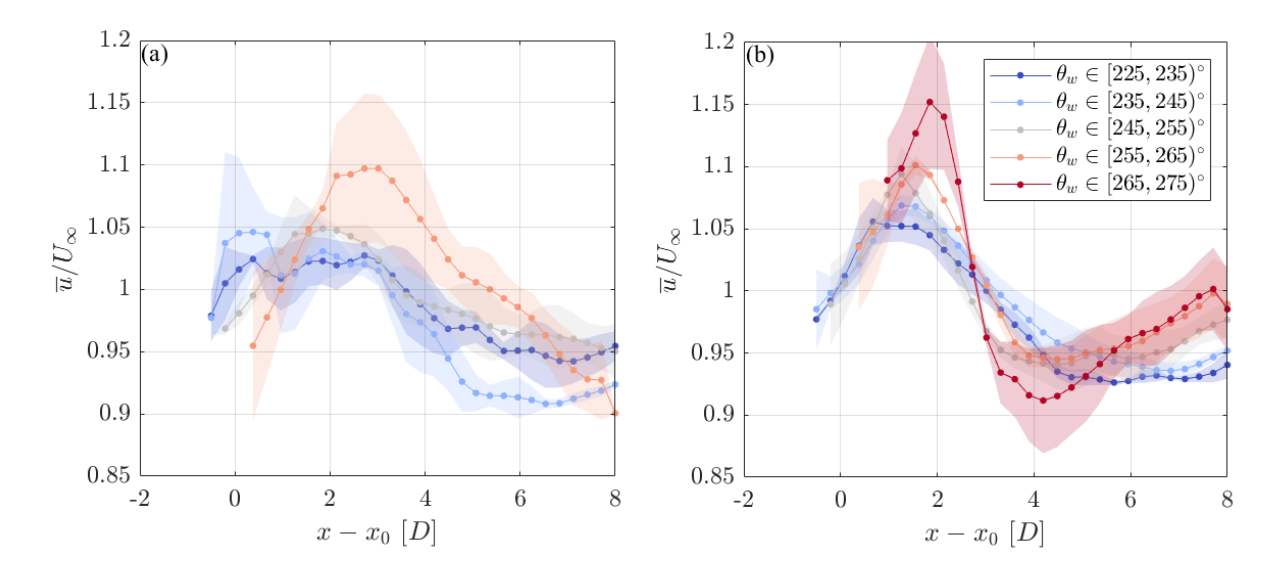


Figure 7. Average streamwise normalized mean velocity between the turbines estimated over the transects reported in Fig. 6: (a) nighttime; (b) daytime. The streamwise coordinate is x, with origin in  $x_0$  (the location of the most upstream turbine for each transect), and positive for locations downstream to the turbine rotor. The shaded regions indicate standard deviation among the different transects.

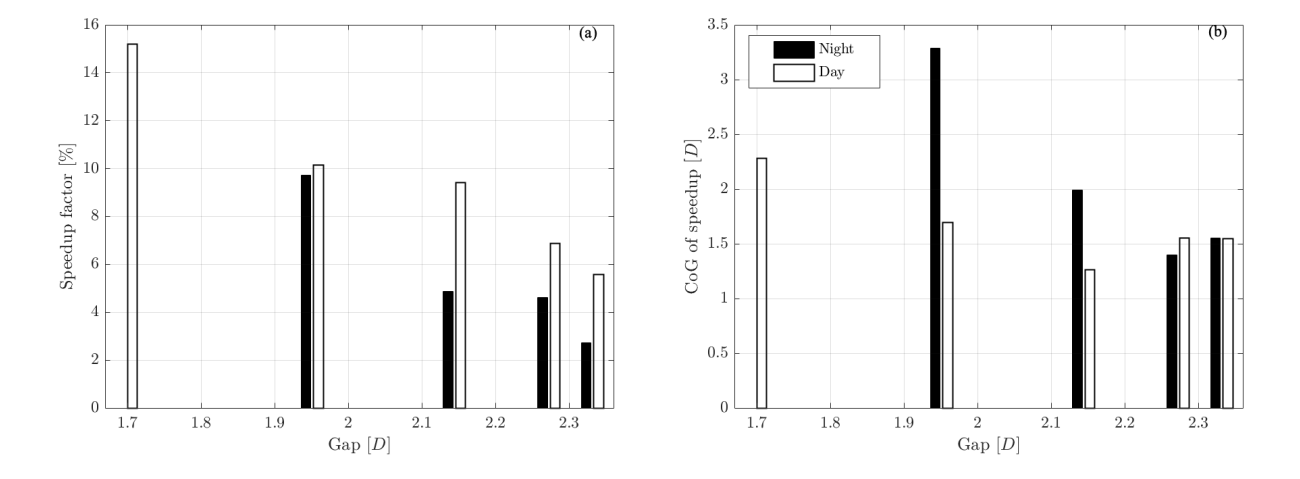


Figure 8. Speedup factor (a) and center of gravity (b).

a downstream distance larger than 1D, which suggests that the speedup regions might have limited effects on the power capture of the turbines generating this flow feature. The analysis of the power performance of the turbines under investigation will be the scope of future work.

### 4. Conclusions

A field campaign was conducted to investigate the effects induced by the thrust force of wind turbine rotors on the incoming wind field. Specifically, the pressure field associated with the rotor thrust of individual wind turbines, or collectively from a turbine array, induces modifications in

**2265** (2022) 022033

doi:10.1088/1742-6596/2265/2/022033

the modulus and direction of the wind velocity while approaching and flowing past the turbine rotors. The main pressure-induced effects may result in velocity reduction in front of the rotor area, which is dubbed as blockage. This flow phenomenon can vary in terms of intensity and upwind extent depending on the thrust coefficient of the turbine and the characteristics of the incoming wind field. Concurrently, the wind field is accelerated while circumventing the turbine rotors. This flow speedup is enhanced when a channeling effect is produced in presence of contiguous wind turbines with limited transverse distance and in presence of wakes leading to a confinement of the freestream. Nonetheless, the three-dimensional characteristics of the incoming boundary layer, generally enhanced during stable atmospheric conditions, and the typical non-stationarity of turbine operations make these flow features difficult to be predicted.

For this study, five profiling wind LiDARs and one scanning Doppler wind LiDAR were deployed before and after the construction of a turbine array over relatively flat terrain. Turbine operations were monitored through the SCADA. The pre-construction LiDAR data has enabled the characterization of the site wind map, namely the quantification of velocity gradients in the streamwise and transverse directions for different wind and atmospheric conditions. This task has resulted to be crucial to correct the post-construction LiDAR data, then characterize rotor-thrust-induced flow features.

The data collected from the profiling LiDARs during wind turbine operations have captured evidence of velocity reductions upstream of wind turbine rotors, which generally increase moving from the top tip towards the bottom tip of the turbine rotor. The velocity reductions are also enhanced under unstable atmospheric conditions with a maximum flow reduction of 5% of the incoming wind speed. Furthermore, flow speedups of about 1% of the incoming wind speed have been observed just aloft of the rotor top tip, which might be the result of the incoming wind field circumventing the turbine rotor.

Due to logistics reasons, the scanning wind LiDAR monitored mainly the area surrounding the turbine rotors and the wakes, rather than the upstream region that might be affected by blockage. Speedups of the incoming wind have been observed for regions between consecutive wind turbines, achieving values as high as 15% of the incoming wind speed under convective conditions. However, the speedup regions have a longer streamwise extent for operations under stable atmospheric conditions, which might be the result of a channeling effect of the further persisting wakes occurring in presence of an incoming turbulence intensity lower than 5%. The center of gravity of the speedup regions is generally located at downstream positions larger than one rotor diameter, which might suggest that flow speedups can produce small effects on the power capture of the wind turbines generating this flow feature.

### Acknowledgments

This material is based upon work supported by the National Science Foundation (grant no. IIP-1362022; Collaborative Research – I/UCRC for Wind Energy, Science, Technology, and Research) and from the WindSTAR I/UCRC Members of Aquanis, Inc., EDP Renewables, Bachmann Electronic Corp., GE Energy, Huntsman, Hexion, Leeward Asset Management, LLC, Pattern Energy, EPRI, LMWind, Texas Wind Tower, and TPI Composites. This research has been partially funded by the National Science Foundation CBET Fluid Dynamics, Program Manager Ron Joslin (Grant No. 1705837, No. 2046160). The presenting author is grateful to the Center for Wind Energy at UT Dallas for providing partial support for conference registration and travel.

### References

- [1] Barthelmie R J, Pryor S C, Frandsen S T, Hansen K S, Schepers J G, Rados K, Schelz W, Neubert A, Jensen L E and Neckelmann S 2010 J. Atmos. Ocean. Tech. 27 1302–1317
- [2] Hansen K S, Barthelmie R J, Jensen L E and Sommer A 2015 Wind Energy 15 183–196

**2265** (2022) 022033

doi:10.1088/1742-6596/2265/2/022033

- [3] El-Asha S, Zhan L and Iungo G V 2017 Wind Energy 20 1823–1839
- [4] Zhan L, Letizia S and Iungo G V 2019 Wind Energy 23 1–27
- [5] Bleeg J, Purcell M, Ruisi R and Traiger E 2018 Energies 11 1–20
- [6] Sebastiani A, Segalini A, Castellani F and Crasto G 2020 Wind Energy 24 1–15
- [7] Schneemann J, Theuer F, Rott A, Dörenkämper M and Kühn M 2021 Wind Energy Sci. 6 521–538
- [8] Nishino T and Willden R H 2012 J. Fluid Mech. 708 596-606
- [9] Nishino T and Draper S 2015 Local blockage effect for wind turbines J. Phys.: Conf. Ser. vol 625 p 012010
- [10] Meyer Forsting A R, Troldborg N and Gaunaa M 2017 Wind Energy 20 63-77
- [11] McTavish S, Rodrigue S and Feszty D 2014 Wind Energy 18 1989–2011
- [12] Lanzilao L and Meyers J 2020 Wind Energy Sci. Disc. 2020 1–30
- [13] Sanchez Gomez M, Lundquist J, Mirocha J, Arthur R and Muñoz-Esparza D 2021 Wind Energy Sci. Disc. 1–21
- [14] Iungo G V, Wu Y T and Porté-Agel F 2013 J. Atmos. Ocean. Technol. 30 274 287
- [15] Debnath M, Iungo G V, Ashton R, Brewer W A, Choukulkar A, Delgado R, Lundquist J K, Shaw W J, Wilczak J M and Wolfe D 2017 Atmos. Meas. Tech. 10 431–444
- [16] Debnath M, Iungo G V, Brewer W A, Choukulkar A, Delgado R, Gunter S, Lundquist J K, Schroeder J L, Wilczak J M and Wolfe D 2017 Atmos. Meas. Tech. 10 1215–1227
- [17] Letizia S, Zhan L and Valerio Iungo G 2021 Atmos. Meas. Tech 14 2065–2093
- [18] Letizia S, Zhan L and Valerio Iungo G 2021 Atmos. Meas. Tech 14 2095–2113
- [19] International Electrotechnical Commission, 61400-12-2 2013 Wind turbine generator systems Part 12-2: Power performance of electricity-producing wind turbines based on nacelle anemometry International Standard 61400-12-2 International Electrotechnical Commission (IEC) Geneva, Switzerland, 2013.
- [20] Larsen G C and Hansen K S 2014 J. Phys.: Conf. Ser. 555
- [21] Branlard E, Quon E, Meyer Forsting A R, King J and Moriarty P 2020 J. Phys. Conf. Ser. 1618 062036
- [22] Branlard E and Forsting A R M 2020 Wind Energy 1–19
- [23] Beck H and Kühn M 2017 Remote Sens. 9 561
- [24] Türk M and Emeis S 2010 J. Wind Eng. Industr. Aerodyn. 98 466-471
- [25] Iungo G V and Porté-Agel F 2014 J. Atmos. Ocean. Technol. 31 2035–2048
- [26] Abkar M and Porté-Agel F 2015 Phys. Fluids 27 035104
- [27] Zhan L, Letizia S and Iungo G V 2020 Wind Energy Sci. 5 1601–1622
- [28] Abkar M, Sørensen J N and Porté-Agel F 2018 Energies 11 1–10